Learning Icosahedral Spherical Probability Map Based on Bingham Mixture Model for Vanishing Point Estimation

Haoang Li[1,*] Kai Chen[1,*] Pyojin Kim[2] Kuk-Jin Yoon[3] Zhe Liu[4] Kyungdon Joo[5,†] Yun-Hui Liu[1,†]
[1]The Chinese University of Hong Kong, Hong Kong, China [2]Sookmyung Women's University, South Korea
[3]KAIST, South Korea [4]University of Cambridge, United Kingdom [5]UNIST, South Korea

Abstract

Existing vanishing point (VP) estimation methods rely on pre-extracted image lines and/or prior knowledge of the number of VPs. However, in practice, this information may be insufficient or unavailable. To solve this problem, we propose a network that treats a perspective image as input and predicts a spherical probability map of VP. Based on this map, we can detect all the VPs. Our method is reliable thanks to four technical novelties. First, we leverage the icosahedral spherical representation to express our probability map. This representation provides uniform pixel distribution, and thus facilitates estimating arbitrary positions of VPs. Second, we design a loss function that enforces the antipodal symmetry and sparsity of our spherical probability map to prevent over-fitting. Third, we generate the ground truth probability map that reasonably expresses the locations and uncertainties of VPs. This map unnecessarily peaks at noisy annotated VPs, and also exhibits various anisotropic dispersions. Fourth, given a predicted probability map, we detect VPs by fitting a Bingham mixture model. This strategy can robustly handle close VPs and provide the confidence level of VP useful for practical applications. Experiments showed that our method achieves the best compromise between generality, accuracy, and efficiency, compared with state-of-the-art approaches.

1. Introduction

Vanishing point (VP) is the intersection of two image lines whose corresponding 3D lines are parallel. VP has various applications such as scene understanding [12], camera orientation estimation [14] and 3D reconstruction [13]. While VP estimation has been widely studied, existing approaches have two main limitations. First, numerous methods [25, 24, 22, 33, 1, 18] rely on pre-extracted image lines, but they are sensitive to the number and quality of lines. For example, given a small number of lines, a method may neglect some VPs (see Figs. 1(a) and 1(b)). Moreover, given several lines corrupted by outliers, e.g., shadow boundaries, a method may mistakenly detect VPs (see Figs. 1(a) and 1(c)). Second, many methods [4, 39, 25, 24, 41] rely on prior knowledge of the number of VPs. They typically assume three orthogonal VPs in Manhattan world [9], and thus neglect partial VPs or result in redundant detection in non-Manhattan scenes [30, 38] (see Figs. 1(a) and 1(d)). While recent approaches [15, 22, 23, 18] can automatically determine the number of VPs, they rely on image lines.

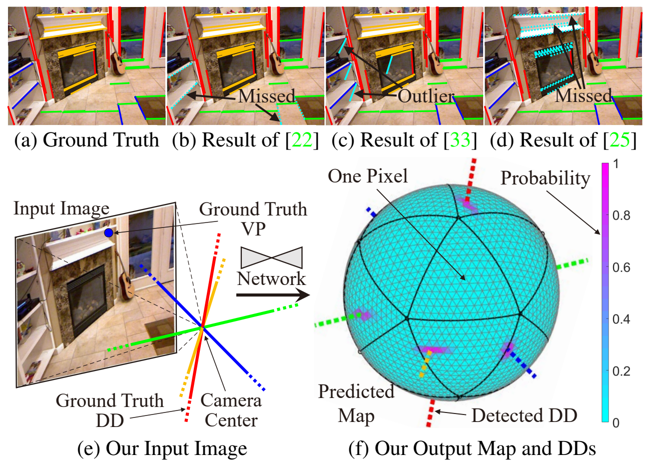

Figure 1. (a) Four ground truth VPs are associated with red, green, blue and yellow line clusters, respectively (we have filtered out short lines). (b) [22] neglects a VP associated with dotted cyan lines due to insufficient lines. (c) [33] mistakenly detects a VP associated with solid cyan outliers. (d) [25] neglects a VP associated with dotted cyan lines due to the assumption of three orthogonal VPs. (e, f) We reformulate VP estimation as DD computation. Given a perspective image, our network predicts a spherical probability map of DD. Based on this map, we can detect all the DDs.

To overcome the above limitations, we propose the first VP estimation method that is independent of image lines and also can automatically determine the number of VPs. Specifically, as shown in Fig. 1(e), the connection between a VP and camera center is aligned to a dominant direction (DD). Compared with VP that may be extremely far from

*Haoang Li and Kai Chen contributed equally to this work.
†Kyungdon Joo and Yun-Hui Liu are corresponding authors.

the image center, unit DD starting at the camera center is enclosed by a unit sphere. We thus follow [41, 22] to reformulate VP estimation as DD computation, i.e., we aim to determine which positions on the sphere correspond to DDs. To achieve this goal, we propose a network that treats a perspective image as input and predicts a spherical probability map of DD. Based on this map, we can detect all the DDs, regardless of the number of DDs.

Our method is reliable thanks to four technical novelties. First, as shown in Fig. 1(f), we leverage the icosahedral spherical representation [2] to express our probability map.[1] This representation provides a more uniform pixel distribution than the widely-used equi-angular discretization on the sphere (see Fig. 2(a)). Accordingly, it facilitates estimating arbitrary orientations of DDs. Second, we design a loss function that not only is effective in fitting data, but also enforces the antipodal symmetry and sparsity of our spherical probability map for regularization. Third, we generate the ground truth map that reasonably expresses the locations and uncertainties of DDs. This map unnecessarily peaks at noisy annotated DDs and also exhibits various anisotropic dispersions (see Fig. 6(d)). We train our network by minimizing the difference between the predicted and ground truth probability maps. Fourth, given a predicted probability map, we detect DDs by fitting a Bingham mixture model [6] (see Fig. 1(f)). This strategy is free of threshold, and thus can handle close DDs more robustly than non-maximum suppression [27]. Moreover, it can provide the confidence level of DD useful for practical applications. Our main contributions are:

- Our method is independent of image lines and also can automatically determine the number of DDs.
- We leverage the icosahedral spherical representation to express our probability map. This representation facilitates estimating arbitrary orientations of DDs.
- We design a loss function that enforces the antipodal symmetry and sparsity of our spherical probability map to prevent over-fitting.
- We introduce a strategy to generate the ground truth probability map that reasonably expresses the locations and uncertainties of DDs.
- We detect DDs by fitting a Bingham mixture model on a predicted map. This strategy is free of threshold and can provide the confidence level of DD.

2. Related Work

We classify existing VP estimation methods into two categories, i.e., traditional and deep learning-based ones.

[1]To the best of our knowledge, we first introduce icosahedral spherical representation to VP estimation problem. Our work may inspire the community to apply this representation to the other geometric problems, e.g., camera pose estimation.

Traditional Methods. Most traditional methods rely on pre-extracted image lines, i.e., they cluster these lines by unknown-but-sought VPs. Representative approaches [28, 3, 39, 33, 4, 5, 25, 24] assume three orthogonal VPs in Manhattan world. Among them, the sampling-based methods [3, 39] hypothesize several candidate VP triplets and select the optimal one that maximizes the number of inlier lines. They lead to unsatisfactory accuracy since some sampled lines may be affected by noise. The search-based methods [4, 5] search in a parameter space related to rotation and find the optimal parameters that maximize the number of inlier lines. They are accurate but inefficient due to numerous rounds of space sub-division and time-consuming bound computation. A method hybridizing the sampling and search [25] achieves a balance between accuracy and efficiency. Due to the assumption of three VPs, the above methods are prone to neglecting partial VPs or resulting in redundant detection in non-Manhattan scenes. In contrast, recent approaches [15, 22, 23] can automatically determine the number of VPs. However, they lead to unsatisfactory efficiency since their parameter spaces are high-dimensional and their cost functions are highly non-linear.

Deep Learning-based Methods. Earlier method [38] requires pre-extracted image lines. It first uses a network to predict several candidate horizons, and then finds the optimal VPs that maximize the number of inlier lines. Recently, some approaches that do not rely on image lines are proposed [8, 41]. They directly treat an image as input. For example, Chang et al. [8] formulated VP estimation as a classification problem. However, this method can only detect VPs within the image. Zhou et al. [41] adopted a coarse-to-fine strategy to sample points on the sphere. For each sampled point, they used a network to predict the probability of VP. Then they selected the points with top K probabilities (K is the number of VPs). While this method can handle VPs outside the image, it is sensitive to the sampling resolution and also requires prior knowledge of the number of VPs. In addition, an approach for multi-model fitting [18] can automatically determine the number of VPs. However, it requires image lines as input.

3. Predicting Spherical Probability Map

Given a perspective image, our network predicts a spherical probability map of DD. In Section 3.1, we introduce the icosahedral spherical representation that makes our network reliably handle arbitrary orientations of DDs. In Section 3.2, we introduce our network architecture. In Section 3.3, we design a novel loss function that exploits the characteristic of spherical map for regularization.

3.1. Icosahedral Spherical Representation

As shown in Fig. 2(a), the widely-used equi-angular discretization on the sphere [15, 22] results in non-uniform

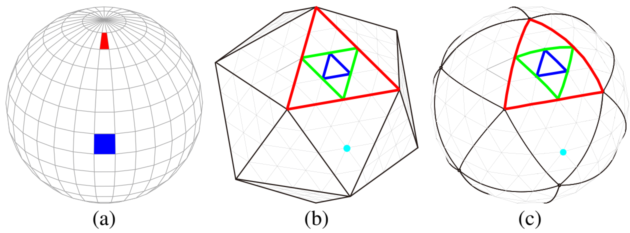

Figure 2. (a) Red and blue faces of the equi-angular discretization on the sphere have different areas. (b) Red triangle is a basic face of icosahedron. Sub-faces obtained by the first and second rounds of sub-divisions are shown in green and blue, respectively. (c) Sub-faces of icosahedral spherical representation are defined by the extruded vertices (e.g., the cyan one) and have similar areas.

pixel distribution. Accordingly, our experiments show that a baseline method using this representation cannot handle arbitrary orientations of DDs, especially DDs near two poles (see Fig. 8(a)). To solve this problem, we propose to use a novel icosahedral spherical representation [2]. As shown in Fig. 2(b), an icosahedron consists of 20 basic faces with the same area. We sub-divide each face into 4 sub-faces. After N rounds of sub-division, we obtain 20×4^N sub-faces. We empirically set N as 5, which leads to reliable DD estimation in our experiments. As shown in Fig. 2(c), we extrude all the vertices of icosahedron sub-faces to the unit sphere, obtaining the icosahedral spherical representation. We use this representation to express our spherical probability map. Specifically, a sub-face of this representation defines a pixel of spherical map. We associate each pixel with the probability that a DD passes through this pixel (see Fig. 1(f)).

In addition, as shown in Fig. 1(f), a DD $\mathbf{d}$ is up to sign, i.e., $\mathbf{d}$ and $-\mathbf{d}$ are equivalent in DD estimation [32]. Accordingly, antipodal pixels of our spherical map should be associated with the same probability of DD. Despite this antipodal symmetry, we do not use the hemisphere to express the probability map. The reason is that a dividing line of sphere, i.e., a great circle (see Fig. 9(a)) may split a probability distribution on the map and further affects the network training, as will be shown in the experiments.

3.2. Network Architecture

As shown in Fig. 3(a), our network is based on encoder-decoder architecture. Our encoder works on the image domain. Given a perspective image, we follow the encoder of well-known DCGAN [29] to obtain a 1024-channel 1D code whose length is 20×4^2. The reason why we choose DCGAN (instead of the other networks) is that DCGAN provides higher reliability in practice. Details are available in the supplementary material. The length of our code equals to the resolution of the icosahedral spherical representation based on two rounds of sub-division. Our decoder works on the sphere domain, and treats our code as the input spherical map. Based on the spherical convolution and up-sampling [20], we alternately extract features (by convolution) and increase the map resolution (by up-sampling). We introduce these operations in the next paragraph. In addition, each spherical convolution is followed by bias adding, batch normalization, and leaky ReLU function. For the one-channel output whose resolution is 20×4^5, we normalize it as a probability map (see Fig. 1(f)) by Sigmoid function.

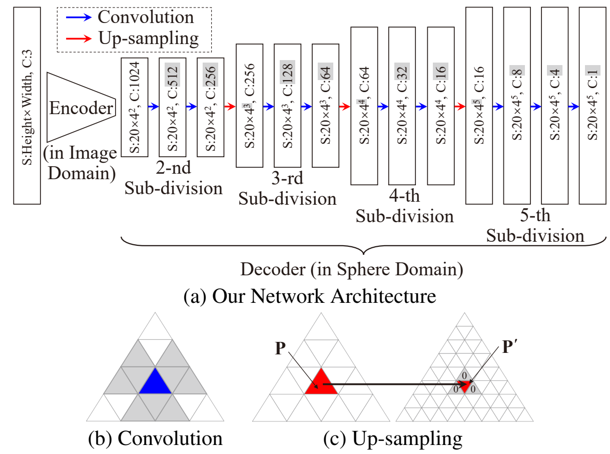

Figure 3. (a) Our network is based on encoder-decoder architecture. "S" and "C" denote the image size and the number of channels, respectively. (b) A pixel and its nine gray neighbors define the shape of convolution kernel. (c) For up-sampling, we transfer a pixel $\mathbf{p}$ in the lower-resolution map to a pixel $\mathbf{p}'$ in the higher-resolution map, and then pad three gray neighbors of $\mathbf{p}'$ with 0.

We consider a pixel of the icosahedral spherical map to illustrate the spherical convolution and up-sampling. As shown in Fig. 3(b), except for the shape of kernel, spherical convolution is similar to image convolution. By setting the stride as 1, convolution does not change the resolution of sphere. As shown in Fig. 3(c), except for the number of neighbors in the higher-resolution map, spherical up-sampling is similar to image up-sampling.

3.3. Loss Function

Our loss function is the combination of three sub-losses. First, we follow [37] to use the pixel-wise mean squared error (MSE) loss. This loss encodes the difference between the predicted and ground truth probability maps. We will introduce how we generate the ground truth map in Section 4. MSE loss is effective in fitting training data. To prevent over-fitting, we exploit the characteristic of probability map for regularization. Specifically, as introduced in Section 3.1, our spherical probability map should exhibit antipodal symmetry. To enforce this constraint, we propose an antipodal symmetry (AS) loss. We define it by the average of the squared differences between all pairs of antipodal pixels on a predicted map. In addition, as shown in Fig. 1(f), many pixels of our probability map should be associated with the probability of 0. To enforce this constraint, we exploit L_0 loss [7] to reduce the number of non-zero pixels. Based on the above sub-losses, we define our total loss by

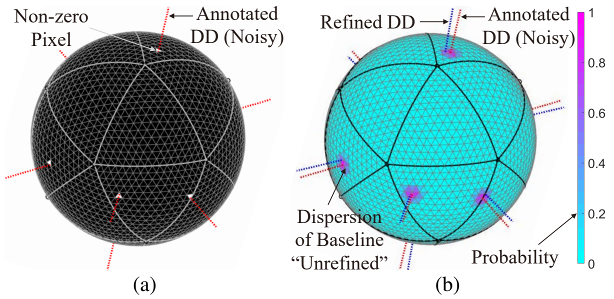

Figure 4. Baselines to generate ground truth maps. (a) Map of Binary. (b) Maps of Unrefined and Refined both follow Watson mixture model [36] whose components exhibit isotropic dispersions. Components of Unrefined peak at noisy annotated DDs, while components of Refined peak at the refined DDs.

$$L = \lambda_{\text{MSE}} \cdot L_{\text{MSE}} + \lambda_{\text{AS}} \cdot L_{\text{AS}} + \lambda_1 \cdot L_0. \tag{1}$$

We empirically set the coefficients λ_{MSE}, λ_{AS} and λ_1 as 2, 0.5 and 0.1, respectively. Our experiments demonstrate the effectiveness of all three sub-losses.

4. Generating Ground Truth Probability Map

Given several annotated DDs[2], we aim to generate the ground truth probability map used in Section 3.2. In the field of VP estimation, a method for spherical ground truth map generation does not exist. We first design various baselines and then propose a reliable method.

4.1. Baselines and Their Limitations

Binary Map (denoted by Binary). We design this baseline by analogy with [40]. Given several annotated DDs, we generate a spherical binary ground truth map. As shown in Fig. 4(a), we assign 1 to the pixels passed by the annotated DDs, and 0 to the other pixels. However, as will be shown in the experiments, due to too high sparsity of this map, the trained network is inaccurate.

Unrefined Watson Mixture Model-based Map (denoted by Unrefined). We design this baseline by analogy with [37]. As shown in Fig. 4(b), we apply Watson distributions [36] with the same isotropic dispersion on pixels passed by the annotated DDs. We choose Watson distribution since its antipodal symmetry is suitable to express DDs (see Section 3.1). This baseline improves the accuracy of the above baseline by reducing the sparsity, as will be shown in the experiments. However, it does consider the noise of annotated DDs, which affects the accuracy. Specifically, on many VP datasets [42, 22, 18], a VP is annotated by computing the intersection of a small number of image lines with the same (manually obtained) labels. It is known that this VP may be unreliable [33, 39], especially when the intersected lines are nearly parallel.

[2]Annotated VPs and DDs can be mutually converted (see Fig. 1(e)).

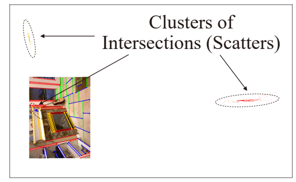

Figure 5. Intersections of all pairs of image lines with the same label constitute a cluster exhibiting anisotropic dispersion. Moreover, dispersions of clusters are different. The cluster generated by green lines is far from the image center and not presented.

Refined Watson Mixture Model-based Map (denoted by Refined). We first follow [33] to alternately refine annotated DDs and update cluster labels of image lines. Then we apply Watson distributions on pixels passed by the refined DDs (see Fig. 4(b)). While this baseline reliably expresses the locations of DDs, it fails to appropriately express the uncertainties of DDs. Specifically, [19] studied the uncertainties of VPs in the image by computing the intersections of all pairs of image lines with the same label. As shown in Fig. 5, the uncertainties of VPs should be expressed by the distributions with various anisotropic dispersions. Similarly, as will be shown in the next section, the uncertainties of DDs should be expressed by the distributions with various anisotropic dispersions. However, Watson distributions used by this baseline exhibit the same isotropic dispersion.

4.2. Map Based on Various Anisotropic Dispersions

To overcome the limitations of the above baselines, we propose a ground truth probability map that appropriately expresses both locations and uncertainties of DDs. First, we follow [33] to alternately refine annotated DDs and update cluster labels of image lines. Then as shown in Fig. 6(a), we map an image line into a great circle on the sphere. As shown in Fig. 6(b), we associate great circles with the updated cluster labels of image lines. As shown in Fig. 6(c), we compute the intersections of all pairs of great circles with the same label. These intersections constitute an antipodally symmetric cluster on the sphere. For all the clusters, their density peaks and various anisotropic dispersions encode the locations and uncertainties of DDs, respectively. Intuitively, a cluster with high-level anisotropic dispersion corresponds to a VP far from the image center.

Based on the intersections computed above, we generate our ground truth probability map. We first define an icosahedral sphere with 20×4^5 sub-faces (see Section 3.1). Then we compute a frequency histogram of intersections over sub-faces of the icosahedral sphere. Specifically, if an intersection lies within a sub-face, we increase the frequency associated with this sub-face by one. Finally, we normalize the frequencies into $[0, 1]$. As shown in Fig. 6(d), we treat the spherical histogram with normalized frequencies as our ground truth probability map. Our map effectively expresses the distribution pattern of intersections.

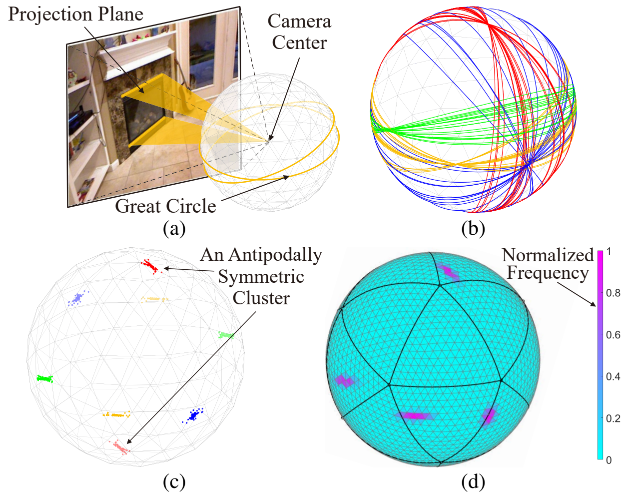

Figure 6. (a) An image line and camera center define a projection plane. This plane intersects with the sphere, generating a great circle. (b) We generate four sets of great circles by the image lines in Fig. 5. (c) Intersections of all pairs of circles with the same label constitute an antipodally symmetric cluster exhibiting anisotropic dispersion. Moreover, dispersions of four clusters are different. (d) We generate a ground truth map by intersections.

5. Detecting DDs Based on Predicted Map

Given a probability map predicted by our network in Section 3.2, we aim to detect DDs. A straightforward way is to use the non-maximum suppression [27]. Briefly, we first select the pixels with high probabilities. Each selected pixel corresponds to a candidate DD. Based on a threshold of angle between two DDs, we sequentially select distinct DDs from candidates in a greedy manner. However, this strategy is relatively sensitive to the above threshold, and thus may result in under- or over-detection (see Figs. 12(d, e)). Moreover, directly selecting a distinct DD without considering its neighbors may result in unsatisfactory accuracy due to the effect of noise. To solve these problems, we propose to detected DDs by fitting a Bingham mixture model [6].

Algorithm Overview. As shown in Fig. 1(f), on our predicted map, there are several antipodally symmetric clusters of non-zero pixels. These clusters exhibit various anisotropic dispersions. Bingham mixture model is suitable to express this pattern. Accordingly, we treat our predicted map as a discrete probability density function of Bingham mixture model and use it to interpolate/fit a model (details are introduced in the next paragraphs). Given a fitted model, we treat the peaks of components as the detected DDs, and treat the concentrations of components as the confidence levels of DDs. These confidence levels are useful for practical applications, e.g., visual SLAM [16] (see the supplementary material). Our method can automatically determine the number of DDs and also robustly handle close DDs, as will be shown in the experiments.

Details of Model Fitting. We first introduce basic knowledge of Bingham mixture model. For a point $\mathbf{g}$ on the sphere, the probability density function of Bingham distribution is given by

$$\mathcal{B}(\mathbf{g}|\mathbf{V},\mathbf{k}) = \frac{1}{f(\mathbf{k})}\exp\Big(\sum_{i=1}^{2} k_i \left(\mathbf{g}^\top \mathbf{v}_i\right)^2\Big), \tag{2}$$

where $\mathbf{v}_1$ and $\mathbf{v}_2$ are basis vectors, and $\mathbf{V} = [\mathbf{v}_1, \mathbf{v}_2]$; k_1 and k_2 are concentration parameters, and $\mathbf{k} = [k_1, k_2]^\top$. A large magnitude of k_i represents that Eq. (2) highly peaks along $\mathbf{v}_i$. To express M Bingham distributions (M represents the unknown-but-sought number of DDs in our context), we use a Bingham mixture model, i.e.,

$$\mathcal{M}(\mathbf{g}) = \sum_{m=1}^{M} c_m \cdot \mathcal{B}(\mathbf{g} \mid \mathbf{V}_m, \mathbf{k}_m), \tag{3}$$

where c_m denotes the mixture coefficient of the m-th component, and satisfies $c_m > 0$ and $\sum_{m=1}^{M} c_m = 1$.

In the following, we introduce the model fitting. We first follow [38] to sample scatters on the sphere based on the predicted probability map. Intuitively, for a pixel associated with large probability, we sample a large number of scatters within this pixel. Given N sampled scatters $\{\mathbf{g}_n\}_{n=1}^{N}$, we aim to cluster them by an unknown-but-sought Bingham mixture model in Eq. (3). To achieve this goal, we maximize a log-likelihood D, i.e.,

$$\underbrace{\max_{M,\,\{\mathbf{V}_m,\mathbf{k}_m,c_m\}_{m=1}^{M}}}_{\text{Model Parameters.}} \underbrace{\log \prod_{n=1}^{N} \mathcal{M}(\mathbf{g}_n)}_{D}. \tag{4}$$

We solve Eq. (4) based on a self-adaptive expectation-maximization algorithm [11]. It can automatically determine the number of DDs M. Specifically, we search M in a reasonable range of the number of DDs, e.g., $[1, 6]$. Given a tentative value $i \in [1, 6]$ of M, we alternately update the cluster labels of scatters and model parameters. Then we back-substitute the estimated parameters into Eq. (4), obtaining the log-likelihood D_i. In addition, we evaluate the complexity of a model with i components by the complexity function $F(i)$ [11]. A small value of $F(i)$ corresponds to low model complexity. By considering both log-likelihood D_i and function $F(i)$, we find the optimal value i based on the minimum message length criterion [35], i.e.,

$$\min_i \big(-D_i + F(i)\big). \tag{5}$$

This criterion controls the trade-off between fitting quality and model complexity. For algorithm initialization, we assign adjacent scatters with the same cluster labels. Experiments show that our algorithm can robustly converge.

6. Experiments

Datasets. Our experiments are on both real-world [10, 22, 18, 31] and synthetic [41] datasets:

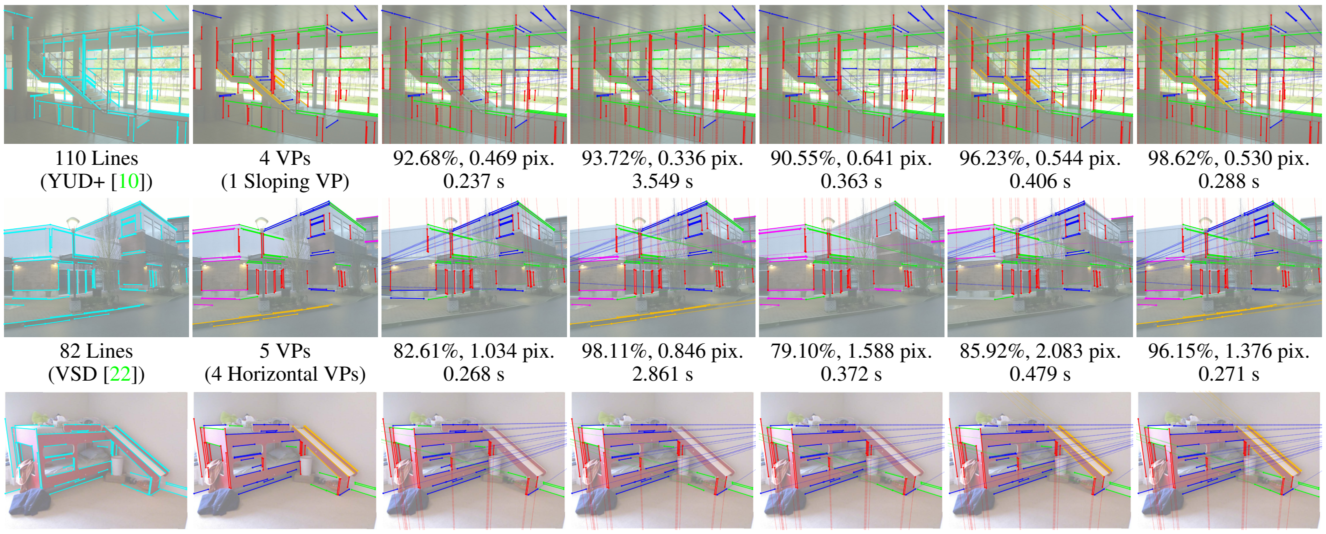

Figure 7. Generality ("**G**"), accuracy ("**A**") and efficiency ("**E**") comparisons on three representative images. "↑", "–" and "↓" represent high, middle and low, respectively. We use image lines to compute F_1-score and consistency error, regardless of whether a method requires image lines for VP estimation. In the 3-rd to 7-th columns, a dotted line in the image represents the connection between the midpoint of a clustered image line and an estimated VP. A triplet of numbers below an image represents F_1-score, consistency error, and run time. Additional comparisons are available in the supplementary material.

Table 1. Generality and accuracy comparisons on various datasets.

Datasets	TR-L-3 [25]		TR-L-auto [22]		DL-nL-3 [41]		DL-L-auto [18]		DL-nL-auto (our)	
	F_1-score	Cons. Error	F_1-score	Cons. Error	F_1-score	Cons. Error	F_1-score	Cons. Error	F_1-score	Cons. Error
YUD+ [10]	79.55%	0.795 pix.	84.18%	0.682 pix.	78.03%	1.832 pix.	87.34%	1.757 pix.	89.43%	1.589 pix.
VSD [22]	75.36%	0.873 pix.	91.02%	0.769 pix.	70.47%	2.008 pix.	88.34%	1.802 pix.	90.76%	1.660 pix.
NYU-VP [31]	80.20%	0.951 pix.	85.73%	0.782 pix.	76.34%	2.078 pix.	86.59%	1.914 pix.	87.88%	1.851 pix.
SU3 [41]	94.88%	0.782 pix.	96.26%	0.598 pix.	94.37%	1.662 pix.	93.89%	1.429 pix.	94.93%	1.478 pix.

- YUD+ [10, 18] consists of 102 outdoor and indoor images with 3∼6 vertical, horizontal and/or sloping VPs.
- VSD [22] consists of 97 outdoor images with 4∼6 vertical and horizontal VPs.
- NYU-VP [31, 18] consists of 1449 indoor images with 1∼6 vertical, horizontal and/or sloping VPs.
- SU3 dataset [41] consists of 23,000 outdoor images with 3∼4 vertical, horizontal and/or sloping VPs.

We extract image lines by LSD [34] to estimate VPs and/or evaluate accuracy. For deep learning-based methods, we treat 80% and 20% of images of each dataset as training and testing images, respectively. We follow [26] to combine all the training images to train a single network. Then we test this network on testing images of each dataset independently. For traditional methods, we test it using the above testing images of each dataset independently. Additional information is available in the supplementary material.

Evaluation Criteria. In our context, high generality represents that a method can detect various VPs, e.g., non-orthogonal horizontal VPs and sloping VPs (see Fig. 7). We follow [22, 21] to evaluate generality by F_1-score that considers both precision and recall of image line clustering. In addition, for accuracy evaluation, we choose the widely-used consistency error [33, 39, 25, 22]. Consistency error in the image is more reasonable than angle evaluation in 3D [41] since uncertainty originates from the image [39]. Specifically, an estimated VP and midpoint of an image line $\mathbf{l}$ associated with this VP define a virtual line $\mathbf{v}$. Consistency error represents the distance from an endpoint of the line $\mathbf{l}$ to the virtual line $\mathbf{v}$. Additional illustrations are available in the supplementary material. On multiple images of a dataset, we report the mean of each metric.

Implementation Details. We use Adam [17] to minimize our loss. Our learning rate is 10^{-4}, batch size is 16, and number of epochs is 30. We implement our method with TensorFlow and conduct tests on a computer equipped with

Table 2. Efficiency comparisons on various datasets.

	YUD+ [10]	VSD [22]	NYU-VP [31]	SU3 [41]
TR-L-3 [25]	0.202 s	0.235 s	0.216 s	0.143 s
TR-L-auto [22]	2.547 s	3.106 s	2.985 s	2.367 s
DL-nL-3 [41]	0.359 s	0.371 s	0.364 s	0.343 s
DL-L-auto [18]	0.383 s	0.477 s	0.401 s	0.268 s
DL-nL-auto (our)	0.268 s	0.279 s	0.284 s	0.271 s

TITAN Xp GPU and Xeon E5-2680 v4 CPU.

6.1. Comparison with State-of-the-art Approaches

We denote our deep learning-based method that does not rely on image lines and also can automatically determine the number of DDs by DL-nL-auto. We compare it with the state-of-the-art approaches introduced in Section 2:

- The traditional method [25] relies on image lines and also assumes 3 mutually orthogonal VPs. We denote it by TR-L-3.
- The traditional method [22] relies on image lines and also can automatically determine the number of DDs. We denote it by TR-L-auto.
- The deep learning-based method [41] does not rely on image lines and also requires prior knowledge of the number of VPs. It assumes 3 VPs when prior knowledge is unavailable. We denote it by DL-nL-3.
- The deep learning-based method [18] relies on image lines and also can automatically determine the number of DDs. We denote it by DL-L-auto.

Generality and Accuracy. As shown in Fig. 7 and Table 1, TR-L-3 only works well in Manhattan world. On the images with non-orthogonal and sloping VPs, it leads to unsatisfactory recall, which affects the F_1-score. TR-L-auto fails to handle sloping VPs and also is prone to neglecting some VPs associated with a small number of image lines. DL-nL-3 can find three non-orthogonal VPs, and thus is more general than TR-L-3. However, it still fails to avoid under- or over-detection of VPs due to the assumption of three VPs. DL-L-auto can hardly detect VPs associated with a small number of image lines due to high difficulty of valid sampling. In contrast, our DL-nL-auto can predict a reliable spherical probability map and detect all the DDs based on this map. In addition, traditional methods lead to smaller consistency error than deep learning-based approaches thanks to geometric constraints. Our DL-nL-auto is the most accurate deep learning-based method.

Efficiency. As shown in Fig. 7 and Table 2, TR-L-3 is not very efficient in non-Manhattan worlds. It treats image lines associated with non-orthogonal VPs as outliers and thus leads to numerous iterations. TR-L-auto is time-consuming due to high-dimensional parameter space and highly nonlinear cost function. The efficiency of DL-nL-3 is moderate due to the simplification of its coarse-to-fine inference strategy. DL-L-auto provides unsatisfactory efficiency for a relatively large number of VPs. Its time cost is mainly caused by sequential computation of sampling weights. Our DL-nL-auto is relatively efficient thanks to concise network and moderate resolution of map. In addition, compared with image line-based methods, deep learning-based approaches lead to smaller variances of runtime.

Table 3. Comparison between icosahedral spherical representation and equi-angular discretization on all the datasets.

	F_1-score	Cons. Error
Equi-angular	79.41%	2.984 pix.
Icosahedral	**90.75%**	**1.644** pix.

Table 4. Comparison between hemisphere and sphere on all the datasets.

	F_1-score	Cons. Error
Hemisphere	88.04%	1.813 pix.
Sphere	**90.75%**	**1.644** pix.

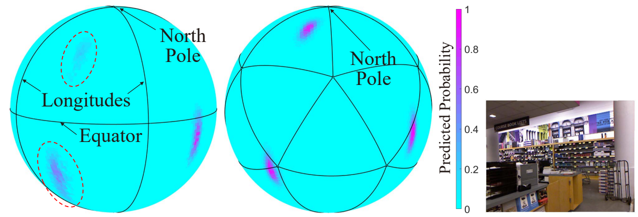

(a) 72.55%, 4.361 pix. (b) 91.03%, 1.573 pix. 3 DDs

Figure 8. Comparison between (a) equi-angular discretization and (b) icosahedral spherical representation on a representative image. A pair of numbers below a sphere represents F_1-score and consistency error. Icosahedral spherical representation is more accurate than equi-angular discretization, especially around two poles.

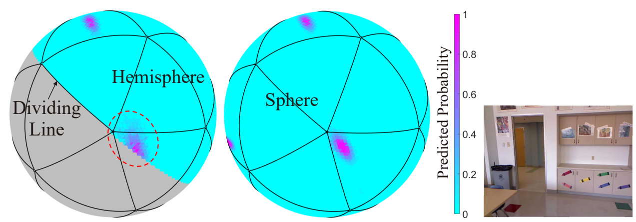

(a) 88.49%, 1.928 pix. (b) 92.56%, 1.360 pix. 3 DDs

Figure 9. Comparison between (a) hemisphere and (b) sphere on a representative image. A pair of numbers below a sphere represents F_1-score and consistency error. Sphere is more accurate than hemisphere, especially around the dividing line.

6.2. Ablation Studies

Spherical Expression. We express our probability map based on icosahedral spherical representation (see Section 3.1). We compare our network based on this representation with a baseline based on the equi-angular discretization. We introduce the architecture of baseline in the supplementary material. For a fair comparison, we set the resolution of equi-angular discretization as $200\times100 = 20,000$ pixels (recall that the icosahedral spherical representation consists of $20 \times 4^5 = 20,480$ pixels). As shown in Table 3 and Fig. 8, icosahedral spherical representation is more accurate than equi-angular discretization. The reason is that this representation provides uniform pixel distribution, and

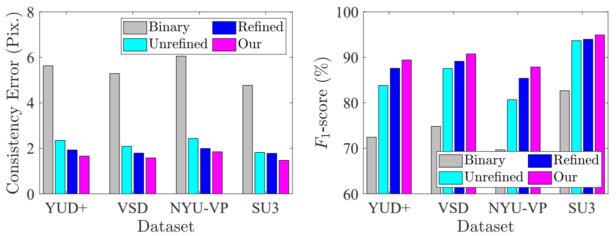

Figure 10. Comparison between various baselines and our method for ground truth map generation on all the datasets.

Table 5. Comparison between various combinations of MSE, AS, and L_0 loess on all the datasets.

	Cons. Error	F_1-score
MSE	1.828 pix.	88.64%
MSE & AS	1.698 pix.	90.02%
MSE & L_0	1.782 pix.	89.37%
MSE & AS & L_0	**1.644** pix.	**90.75%**

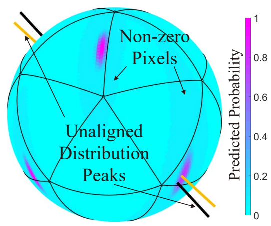

Figure 11. A predicted map obtained by only MSE loss.

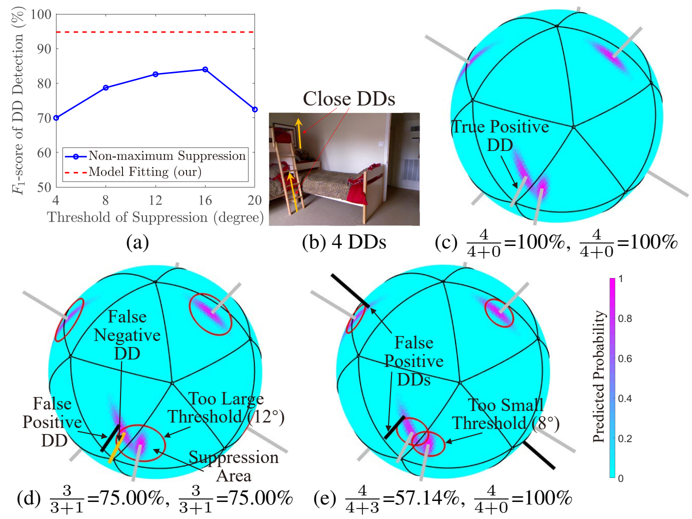

Figure 12. Comparison between non-maximum suppression and our model fitting for DD detection. (a) Results on 156 images with close DDs whose angles are small than 30 degrees. (b) A representative image with two close DDs. (c) DDs detected by our model fitting. (d, e) DDs detected by non-maximum suppression. A pair of numbers below a sphere represents precision and recall of DD detection (except for this figure, precisions, recalls and F_1-scores in the other figures and tables are about image line clustering).

thus facilitates estimating arbitrary orientations of DDs.

In addition, we express the probability map on the sphere instead of hemisphere (see Section 3.1). We use the ground truth maps expressed by sphere and hemisphere to train our network, respectively. Table 4 and Fig. 9 show that sphere leads to higher accuracy. The reason is that sphere can keep the integrity of probability distribution. In contrast, when generating hemisphere, a dividing line of sphere may split a probability distribution. Accordingly, hemisphere results in unreliable probability prediction around the dividing line.

Ground Truth Probability Map. We design baselines Binary, Unrefined and Refined and our method (see Section 4). We use different ground truth maps generated by these methods to train our network. As shown in Fig. 10, Binary leads to low accuracy since too high sparsity of ground truth map affects network training. The accuracy of Unrefined is unsatisfactory since it neglects the noise of annotated DDs. Refined improves the accuracy to some extent. However, due to inappropriate expression of uncertainties of DDs, it can hardly handle VPs far from the image center. Our method provides the highest accuracy since it reasonably expresses both locations and uncertainties of DDs.

Loss Function. Our loss function is the combination of MSE, AS, and L_0 sub-losses (see Section 3.3). We test our network trained by various combinations of sub-losses. Additional tests on coefficient variation are available in the supplementary material. As shown in Table 5 and Fig. 11, MSE loss is effective in fitting the probability maps, but the accuracy is limited by slight asymmetry and too wide dispersions of distributions. AS and L_0 losses both improve the accuracy. The reason is that they can align the peaks of distributions and compress small non-zero probabilities respectively, and thus effectively prevents over-fitting.

DD Detection. We detect DDs by fitting a Bingham mixture model instead of non-maximum suppression (see Section 5). Given the same predicted probability map, we compare these strategies. As shown in Fig. 12, non-maximum suppression is prone to resulting in under- or over-detection especially when two DDs are relatively close. In contrast, our method is robust since it is free of threshold.

7. Conclusions

The proposed VP estimation method is independent of image lines and also can automatically determine the number of VPs, providing high generality. Moreover, it achieves satisfactory accuracy and high efficiency thanks to novel spherical representation, loss function, ground truth map generation, and DD detection. Therefore, it is more practical than existing methods failing to simultaneously guarantee generality, accuracy, and efficiency.

Acknowledgments. Yun-Hui Liu was supported by the Hong Kong Centre for Logistics Robotics, RGC via grant 14207320, the CUHK VC Discretionary Fund, and Shenzhen Municipal Government via the Shenzhen-HK Collaboration Zone Project. **Kyungdon Joo** was supported by Institute of Information & communications Technology Planning & Evaluation (IITP) grant funded by the Korea government (MSIT) (No. 2020-0-01336, Artificial Intelligence Graduate School Program (UNIST)) and the National Research Foundation of Korea (NRF) grant funded by the Korea government (MSIT) (No. NRF-2021R1C1C1005723). **Pyojin Kim** was supported by the National Research Foundation of Korea (NRF) grant funded by the Korea government (MSIT) (No. 2021R1F1A1061397). **Kuk-Jin Yoon** was supported by Institute of Information and Communications Technology Planning & Evaluation (IITP) Grant funded by Korea Government (MSIT) (No. 2020-0-00440, Development of Artificial Intelligence Technology that Continuously Improves Itself as the Situation Changes in the Real World).

References

[1] Michel Antunes and Joao Barreto. A global approach for the detection of vanishing points and mutually orthogonal vanishing directions. In *CVPR*, 2013. 1

[2] John Baumgardner and Paul Frederickson. Icosahedral discretization of the two-sphere. *SIAM Journal on Numerical Analysis*, 1985. 2, 3

[3] Jean-Charles Bazin and Marc Pollefeys. 3-line RANSAC for orthogonal vanishing point detection. In *IROS*, 2012. 2

[4] Jean-Charles Bazin, Yongduek Seo, Cedric Demonceaux, Pascal Vasseur, Katsushi Ikeuchi, Inso Kweon, and Marc Pollefeys. Globally optimal line clustering and vanishing point estimation in Manhattan world. In *CVPR*, 2012. 1, 2

[5] Jean-Charles Bazin, Yongduek Seo, and Marc Pollefeys. Globally optimal consensus set maximization through rotation search. In *ACCV*, 2012. 2

[6] Christopher Bingham. An antipodally symmetric distribution on the sphere. *The Annals of Statistics*, 1974. 2, 5

[7] Christopher Bishop. *Pattern recognition and machine learning*. Springer, 2006. 3

[8] Chin-Kai Chang, Jiaping Zhao, and Laurent Itti. DeepVP: Deep learning for vanishing point detection on 1 million street view images. In *ICRA*, 2018. 2

[9] James Coughlan and Alan Yuille. Manhattan world: Compass direction from a single image by Bayesian inference. In *ICCV*, 1999. 1

[10] Patrick Denis, James Elder, and Francisco Estrada. Efficient edge-based methods for estimating Manhattan frames in urban imagery. In *ECCV*, 2008. 5, 6, 7

[11] Mario Figueiredo and Anil Jain. Unsupervised learning of finite mixture models. *TPAMI*, 2002. 5

[12] Alex Flint, David Murray, and Ian Reid. Manhattan scene understanding using monocular, stereo, and 3D features. In *ICCV*, 2011. 1

[13] Yuan Gao and Alan Yuille. Exploiting symmetry and/or Manhattan properties for 3D object structure estimation from single and multiple images. In *CVPR*, 2017. 1

[14] Jeong-Kyun Lee and Kuk-Jin Yoon. Real-time joint estimation of camera orientation and vanishing points. In *CVPR*, 2015. 1

[15] Kyungdon Joo, Tae-Hyun Oh, In So Kweon, and Jean-Charles Bazin. Globally optimal inlier set maximization for Atlanta world understanding. *TPAMI*, 2019. 1, 2

[16] Pyojin Kim, Brian Coltin, and H Jin Kim. Low-drift visual odometry in structured environments by decoupling rotational and translational motion. In *ICRA*, 2018. 5

[17] Diederik Kingma and Jimmy Ba. Adam: A method for stochastic optimization. In *ICLR*, 2015. 6

[18] Florian Kluger, Eric Brachmann, Hanno Ackermann, Carsten Rother, Michael Ying Yang, and Bodo Rosenhahn. CONSAC: Robust multi-model fitting by conditional sample consensus. In *CVPR*, 2020. 1, 2, 4, 5, 6, 7

[19] Jana Košecká and Wei Zhang. Video compass. In Anders Heyden, Gunnar Sparr, Mads Nielsen, and Peter Johansen, editors, *ECCV*, 2002. 4

[20] Yeonkun Lee, Jaeseok Jeong, Jongseob Yun, Wonjune Cho, and Kuk-Jin Yoon. SpherePHD: Applying CNNs on 360° images with non-Euclidean spherical polyhedron representation. *TPAMI*, 2020. 3

[21] Haoang Li, Kai Chen, Ji Zhao, Jiangliu Wang, Pyojin Kim, Zhe Liu, and Yun-Hui Liu. Learning to identify correct 2D-2D line correspondences on sphere. In *CVPR*, 2021. 6

[22] Haoang Li, Pyojin Kim, Ji Zhao, Kyungdon Joo, Zhipeng Cai, Zhe Liu, and Yun-Hui Liu. Globally optimal and efficient vanishing point estimation in Atlanta world. In *ECCV*, 2020. 1, 2, 4, 5, 6, 7

[23] Haoang Li, Yazhou Xing, Ji Zhao, Jean-Charles Bazin, Zhe Liu, and Yun-Hui Liu. Leveraging structural regularity of Atlanta world for monocular SLAM. In *ICRA*, 2019. 1, 2

[24] Haoang Li, Ji Zhao, Jean-Charles Bazin, Wen Chen, Zhe Liu, and Yun-Hui Liu. Quasi-globally optimal and efficient vanishing point estimation in Manhattan world. In *ICCV*, 2019. 1, 2

[25] Haoang Li, Ji Zhao, Jean-Charles Bazin, and Yun-Hui Liu. Quasi-globally optimal and near/true real-time vanishing point estimation in Manhattan world. *TPAMI*, 2020. 1, 2, 6, 7

[26] Zhengfa Liang, Yulan Guo, Yiliu Feng, Wei Chen, Linbo Qiao, Li Zhou, Jianfeng Zhang, and Hengzhu Liu. Stereo matching using multi-level cost volume and multi-scale feature constancy. *TPAMI*, 2021. 6

[27] Alexander Neubeck and Luc Van Gool. Efficient non-maximum suppression. In *ICPR*, 2006. 2, 5

[28] Long Quan and Roger Mohr. Determining perspective structures using hierarchical Hough transform. *PRL*, 1989. 2

[29] Alec Radford, Luke Metz, and Soumith Chintala. Unsupervised representation learning with deep convolutional generative adversarial networks. In *ICLR*, 2016. 3

[30] G. Schindler and F. Dellaert. Atlanta world: An expectation maximization framework for simultaneous low-level edge grouping and camera calibration in complex man-made environments. In *CVPR*, 2004. 1

[31] Nathan Silberman, Derek Hoiem, Pushmeet Kohli, and Rob Fergus. Indoor segmentation and support inference from RGBD images. In *ECCV*, 2012. 5, 6, 7

[32] Julian Straub, Oren Freifeld, Guy Rosman, John Leonard, and John Fisher. The Manhattan frame model—Manhattan world inference in the space of surface normals. *TPAMI*, 2018. 3

[33] Jean-Philippe Tardif. Non-iterative approach for fast and accurate vanishing point detection. In *ICCV*, 2009. 1, 2, 4, 6

[34] R. Grompone von Gioi, J. Jakubowicz, J. Morel, and G. Randall. LSD: A fast line segment detector with a false detection control. *TPAMI*, 2010. 6

[35] Chris Wallace and David Boulton. An Information Measure for Classification. *The Computer Journal*, 1968. 5

[36] Geoffrey Watson. The statistics of orientation data. *The Journal of Geology*, 1966. 4

[37] Bin Xiao, Haiping Wu, and Yichen Wei. Simple baselines for human pose estimation and tracking. In *ECCV*, 2018. 3, 4

[38] Menghua Zhai, Scott Workman, and Nathan Jacobs. Detecting vanishing points using global image context in a Non-Manhattan world. In *CVPR*, 2016. 1, 2, 5

[39] Lilian Zhang, Huimin Lu, Xiaoping Hu, and Reinhard Koch. Vanishing point estimation and line classification in a Manhattan world with a unifying camera model. *IJCV*, 2016. 1, 2, 4, 6

[40] Ziheng Zhang, Zhengxin Li, Ning Bi, Jia Zheng, Jinlei Wang, Kun Huang, Weixin Luo, Yanyu Xu, and Shenghua Gao. PPGNet: Learning point-pair graph for line segment detection. In *CVPR*, 2019. 4

[41] Yichao Zhou, Haozhi Qi, Jingwei Huang, and Yi Ma. NeurVPS: Neural vanishing point scanning via conic convolution. In *NeurIPS*, 2019. 1, 2, 5, 6, 7

[42] Zihan Zhou, Farshid Farhat, and James Wang. Detecting dominant vanishing points in natural scenes with application to composition-sensitive image retrieval. *TMM*, 2017. 4